*chemistry*

MDPI

*Article*

# Controlled Assembly of Lipid Molecules via Regulating Transient Spatial Confinement

**Yuqi Huang [1], Umit Celik [1], Ziqian Xu [1], Daniel Speer [2], Dario Ossola [3], Roland Faller [4,5], Atul N. Parikh [6] and Gang-Yu Liu [1,*]**

[1] Department of Chemistry, University of California, Davis, CA 95616, USA; yqhuang@ucdavis.edu (Y.H.); zqnxu@ucdavis.edu (Z.X.)
[2] Chemistry Graduate Group, University of California, Davis, CA 95616, USA; djspeer@ucdavis.edu
[3] Cytosurge AG, 8152 Glattbrugg, Switzerland; dario.ossola@cytosurge.com
[4] Department of Chemical Engineering, University of California, Davis, CA 95616, USA; roland.faller@ttu.edu
[5] Department of Chemical Engineering, Texas Tech University, Lubbock, TX 79409, USA
[6] Department of Biomedical Engineering, University of California, Davis, CA 95616, USA; anparikh@ucdavis.edu
* Correspondence: gyliu@ucdavis.edu

**Abstract:** The constructs of lipid molecules follow self-assembly, driven by intermolecular interactions, forming stacking of lipid bilayer films. Achieving designed geometry at nano- to micro-levels with packing deviating from the near-equilibrium structure is difficult to achieve due to the strong tendency of lipid molecules to self-assemble. Using ultrasmall (<fL) droplets containing designed molecules, our prior work has demonstrated that molecular assembly, in principle, is governed mainly by transient inter-molecular interactions under their dynamic spatial confinement, i.e., tri-phase boundaries during drying. As a result, the assemblies can deviate, sometimes significantly, from the near-equilibrium structures of self-assembly. The present work applies the approach and concept to lipid molecules using 1-palmitoyl-2-oleoyl-*sn*-glycero-3-phosphocholine (POPC). Taking advantage of the high spatial precision and the minute size of the delivery probe in our combined atomic force microscopy and microfluidic delivery, the transient shape of each liquid droplet is regulated. In doing so, the final geometry of the POPC assemblies has been regulated to the designed geometry with nanometer precision. The results extend the concept of controlled assembly of molecules to amphiphilic systems. The outcomes exhibit high potential in lipid-based biomaterial science and biodevice engineering.

**Keywords:** controlled assembly; atomic force microscopy (AFM); lipid; 1-palmitoyl-2-oleoyl-*sn*-glycero3-phosphocholine (POPC); 3D nanoprinting

check for updates

**Citation:** Huang, Y.; Celik, U.; Xu, Z.; Speer, D.; Ossola, D.; Faller, R.; Parikh, A.N.; Liu, G.-Y. Controlled Assembly of Lipid Molecules via Regulating Transient Spatial Confinement. *Chemistry* **2024**, *6*, 1287–1300. https://doi.org/10.3390/chemistry6050074

Academic Editors: Valentine Vullev and Igor Alabugin

Received: 18 September 2024
Revised: 15 October 2024
Accepted: 16 October 2024
Published: 19 October 2024

**Copyright:** © 2024 by the authors. Licensee MDPI, Basel, Switzerland. This article is an open access article distributed under the terms and conditions of the Creative Commons Attribution (CC BY) license (https://creativecommons.org/licenses/by/4.0/).

## 1. Introduction

Lipid constructs at the nano- to micro-scale are of scientific as well as technological significance [1,2]. Local lipid structures in cell membranes impact cellular signaling and communication processes [1,3,4]. Lipid assemblies at the mesoscale have also revealed new structural characteristics and phase behavior [5–8]. Due to high biocompatibility, flexibility, and biodegradability, lipid assemblies have been widely used in drug delivery [9], biosensing [10,11], and, as key components, biomaterials [12–14]. The high stability of many lipid assemblies leads to applications in modern biodevices, as well as on-chip assays [15].

Engineering lipid constructs are typically based on self-assembly, e.g., using drop-casting [16], Langmuir–Blodgett (LB) techniques [17,18], or vesicle fusion [19]. These methods have the advantages of simplicity of operation and relatively high throughput. Principle limitations include difficulties in miniaturizing into nano- and micro-scales and broad distribution of feature size and shapes. Since molecular packing is mainly dependent on the self-assembly of lipid molecules due to their strong inter-molecular interactions, it

is difficult to produce off-equilibrium structures by design with nanometer precision [20]. The need for miniaturing lipid constructs by design sparks alternative approaches such as atomic force microscopy (AFM)-based nanografting [21], dip-pen nanolithography (DPN) [22–25], and microcontact printing (μCP) [26,27], all of which are intrinsically 2D nanolithography. Layer-by-layer delivery into 3D constructs by design remains challenging using these 2D-based technologies, mainly due to the difficulty in attaining inter-layer registry and accurate delivery at the nanometer scale.

Recently, the concept of "controlled assembly of molecules" was introduced by our team to address those challenges [28]. A state-of-the-art, combined AFM and microfluidic delivery system was used to deliver ultrasmall droplets onto designated surfaces, as illustrated in Figure 1A [28–31]. The AFM setup differs from conventional AFMs in that layer-by-layer delivery with nanometer precision is enabled [29,32,33]. A separately controlled z-movement in conjunction with a small microfluidic delivery probe enables the delivery of liquid droplets as small as 0.4 attoliters (aL) [28,34,35]. Ultrafast evaporation and spatial confinement by small droplets are keys to controlling the assembly of solute molecules. The rapid evaporation locks solute molecules in their transient locations, leading to features with locally driven geometries [28,29]. The concept of controlled assembly of molecules has been demonstrated in our previous work via the formation of various assemblies of star polymers and fluorenyl methoxycarbonyl (Fmoc)-tagged heparosan tetrasaccharide (referred to as "heparosan") [28,29]. Star polymers exhibited repulsive intermolecular interactions [28], and heparosan had a weak intermolecular attraction in solutions [29]. Therefore, the assembly of these molecules was primarily dictated by the transient dynamic factors, such as the spatial confinement of the ultrasmall droplet during drying. Lipid molecules, in comparison, are amphiphilic with a stronger tendency than prior systems to self-assemble, e.g., forming bilayers or a bilayer stack due to strong intermolecular interactions (e.g., free energy barrier ~23 kJ/mol for water permeation) [36]. Thus, a fundamental question remains whether this approach could be utilized to control the assembly of lipid molecules, i.e., if the dynamic confinement and rapid evaporation could impact or overcome the intermolecular interactions and dictate lipid assemblies.

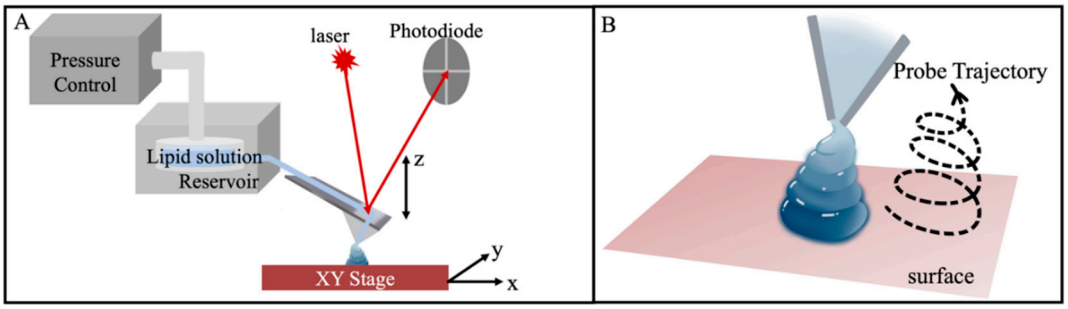


**Figure 1.** (**A**) Schematic diagram of a combined AFM with a microfluidic delivery probe. (**B**) A schematic illustrates the capability of moving the probe following a designed trajectory during the delivery and drying of a single droplet.

This work applies the concept and technology of controlled assembly of molecules to lipid molecules, using 1-palmitoyl-2-oleoyl-*sn*-glycero-3-phosphocholine (POPC). POPC represents a phospholipid that is commonly used in biochemical and biophysical research due to its natural abundance in cell membranes [37,38], taking advantage of the high spatial precision and the minute size of the delivery probe tip in a combined atomic force microscopy and microfluidic system (Figure 1A). A similar combination has been reported previously to produce 3D lipid patterns, including pure and composite lipid constructs (lipid inlaid with cholesterol) [32,39,40]. The size of the 3D construct depends on the delivery conditions, such as contact time, probe dimension, and delivery pressure [32,39]. Complimentary to these prior efforts, this work regulates the transient shape of the liquid droplet by dynamic tip movement upon dispensing and during drying, as illustrated in

Figure 1B. In doing so, the shape of the final POPC assembly can be regulated to designed geometries with nanometer precision in all three dimensions. In contrast to our prior approach of controlled assembly of molecules [28–31], which delivered a liquid droplet and let it naturally dry, this work actively perturbs the transient geometry of the liquid droplet during drying, thus enabling structures beyond surface-tension-driven shapes, as the final assembly of POPC is dictated by the transient location of individual molecules and their local environments at the moment of drying. These results validate and extend the concept of "controlled assembly of molecules" to amphiphilic systems. The outcomes pave the way for the 3D nanoprinting of lipids and the engineering of lipid-based biomaterials and nanobiodevices.

## 2. Materials and Methods

### *2.1. Materials and Supplies*

Glass slides and glass coverslips were purchased from Fisher Scientific (Pittsburgh, PA, USA). Reagents were used without further purification. Glycerol (>99%), sulfuric acid ($H_2SO_4$, 95.0–98.0%), hydrogen peroxide ($H_2O_2$, 30% aqueous solution), ammonium hydroxide ($NH_4OH$, 28.0–30.0% aqueous solution), and chloroform (99.8%) were purchased from Sigma-Aldrich (St. Louis, MO, USA). Octadecyltrichlorosilane (OTS) was purchased from Gelest (Morrisville, PA, USA). Ethanol (200 Proof pure ethanol) was purchased from Koptec (King of Prussia, PA, USA). Milli-Q water (MQ water, 18.2 MΩ·cm at 25 °C) was produced by a Milli-Q water purification system (EMD Millipore, Billerica, MA, USA). Nitrogen gas (99.999%) was purchased from Praxair, Inc. (Danbury, CT, USA; King of Prussia, PA, USA). 1-palmitoyl-2-oleoyl-*sn*-glycero-3-phosphocholine (POPC) and 1,2-dioleoyl-sn-glycero-3-phosphoethanolamine-*N*-(7-nitro-2-1,3-benzoxadiazol-4-yl) (NBD-PE) were purchased from Avanti Lipids, Inc. (Alabaster, AL, USA). The sterile specimen containers (REF354014) were purchased from Corning (NY, USA).

### *2.2. Preparation of Self-Assembled Monolayers on Glass and Probe Surfaces*

Two surface classes were used as support for this work: clean and modified glass coverslips. Clean coverslips were first cleaned with ethanol, then water, followed by plasma treatment for five minutes with a plasma cleaner (PDC-32G, Harrick Plasma, Ithaca, NY, USA). Clean coverslips were used for sample preparation immediately after plasma treatment. To prepare the modified cover slips, e.g., OTS self-assembled monolayers (SAMs) on glass coverslips, the glass coverslips were first cleaned following established protocols [28,41–45]. Briefly, the glass coverslip was cleaned by first soaking them in piranha solution ($H_2SO_4$:$H_2O_2$ = 3:1 $v/v$) for 1 h. The coverslips were then rinsed with copious amounts of MQ water before being soaked in a basic bath, which contained $NH_4OH$, $H_2O_2$, and MQ water at a ratio of 5:1:1 ($v/v/v$) for 1 h in an oven (VMR Scientific Products, Tempe, AZ, USA) heated to 70 °C. Finally, the clean glass coverslips were rinsed again with a copious amount of MQ water and dried using nitrogen gas. The OTS self-assembled monolayers (SAMs) on clean glass coverslips were prepared shortly before use. Briefly, the clean glass coverslips were placed into a sealed specimen container (100 mL) containing 225 µL of OTS and heated at 70 °C in the oven for 2 h. The modified coverslips were rinsed with ethanol and dried in nitrogen gas.

The OTS-coated probe was prepared by first plasma-cleaning a new FluidFM nanopipette (Cytosurge, Glattbrugg, Switzerland) for 1 min; then the probe was placed into a sealed specimen container (100 mL) containing 150 µL of OTS and heated in the oven at 70 °C for 1 h. This protocol yields a self-assembly monolayer of OTS on silica surfaces, including glass slides and silicon wafers [29,42,43,45].

### *2.3. Contact Angle Measurements*

Contact angles were measured using a VCA Optima Contact Angle Measurement System (AST Products, Billerica, MA, USA), following well-established protocols [28,29,46–48]. A total of 3 µL of designated liquid was dispensed on the surface using a high-performance

liquid chromatography (HPLC) needle (700 series, Hamilton Co., Reno, NV, USA). At least three different locations per sample were measured to ensure consistency and reproducibility.

### *2.4. Combined Atomic Force Microscopy and Microfluidic Delivery*

The delivery process was carried out by using a FluidFM BOT (Cytosurge, Glattbrugg, Switzerland), an Atomic Force Microscopy (AFM)-based microfluidic delivery platform [33,49]. Key components include an inverted optical microscope (IX-73, Olympus America, Center Valley, PA, USA), a nanopipette with a 300 nm opening connected to the material reservoir, control units for AFM probe contact and positioning, as well as material delivery (pressure ranging from −800 mbar to 1000 mbar, and precise millisecond-level control of contact time) [39,49–51]. The long-range XY-stage has a movable X range of 240 mm and Y range of 74.5 mm, with absolute stage repeatability down to 500 nm [32,49,52]. This setup can accommodate a wide range of materials, from genuine solutions to glue-like materials [28,29,52]. After delivery, the samples are kept in a clean environment and under ambient laboratory conditions for storage until characterization. The laboratory temperature and humidity are controlled at 22.5 ± 0.5 °C and 40 ± 2%, measured by a digital hygrometer (TP50, ThermoPro, Duluth, GA, USA), respectively.

### *2.5. Atomic Force Microscopy Imaging*

The POPC constructs were left to air dry and imaged on an AFM (MFP-3D, Oxford Instrument, Santa Barbara, CA, USA). Microfabricated silicon nitride probes (MSNL-10 E, Bruker, Camarillo, CA, USA) were used to characterize the lipid structures produced in this work. Images were acquired using tapping mode with 60–78% damping [29,32,53]. Imaging processing, analysis, and display were carried out using the MFP-3D software developed on the Igor Pro 6.20 platform (WaveMetrics, Lake Oswego, OR, USA).

### *2.6. Laser Scanning Confocal Microscopy Imaging*

A laser scanning confocal microscope (FV-1000, Olympus America, Center Valley, PA, USA) was utilized. A 10× bright field objective was used for visualizing the lipid patterns. Argon laser excitations at 458 nm and 535–635 nm emission windows were utilized to collect the NBD-PE fluorescent signal [54]. The images were taken at 10 µs/pixel scanning speed and 800 × 800 pixels in each image. Imaging processing and display were performed using the FV10-ASW Viewer software (Ver. 4.2b, Olympus America, Center Valley, PA, USA).

## 3. Results and Discussion

### *3.1. Control Over the Shape of Individual Lipid Constructs*

Figure 2 reveals that symmetric shapes of lipids can be constructed by varying initial delivery conditions, e.g., droplet shape and size, concentration of POPC, and solvo-philicity of the surface. To prepare the lipid stock solutions, POPC was first dissolved in chloroform in preparation for a POPC stock solution of $3.3 \times 10^{-2}$ M. NBD-PE stock solution was made by dissolving NBD-PE in chloroform at a concentration of $5.2 \times 10^{-3}$ M. 39.5 µL of POPC stock solution and 2.5 µL NBD-PE stock solution were then mixed, and the mixture was then dried in nitrogen atmosphere, resulting in a yellow-colored POPC/NBD-PE solid mixture. Immediately before each delivery experiment, the POPC/NBD-PE mixture was redissolved in 40 µL of a mixed solvent, ethanol:glycerol ($v$:$v$ = 9:1), reaching a final concentration [POPC] = $3.3 \times 10^{-2}$ M, [NBD-PE] = $3.3 \times 10^{-4}$ M, i.e., dye:POPC = 1:100. A plasma-cleaned glass slide was used, whose contact angle measured as near zero for the POPC solutions. Delivery was carried out at extrusion pressure $p$ = 10 mbar and contact duration t = 10 ms, with contact force F = 49 nN. A 3 × 3 array was first produced. Figure 2A reveals an example in which POPC molecules assembled into a disk with a diameter of 1.66 ± 0.02 µm and height of 39.2 ± 0.8 nm. The disk shape is consistent with the mechanism of constant-area evaporation due to the solvo-philic nature of the surface [28,55–57]. In the constant-area evaporation-driven molecular assembly, the disk

diameter is defined by the diameter of the interfacial circle of the original droplet, which adopted a spherical cap geometry. During the evaporation, inter-molecular interactions dictate the outcome of lipid packing within the feature, i.e., bilayers stacking atop each other, as illustrated in Figure 2B. The high solute concentration and sufficient time of interactions ensured inter-molecular interaction-driven outcomes. The robustness was demonstrated by forming wider and taller lipid disks using longer delivery time and higher extrusion pressure. For instance, under $p$ = 300 mbar and t = 10 ms, POPC disks measured 2.52 ± 0.07 µm in diameter and 174 ± 0.7 nm in height (Figure S1). Extending t = 500 ms, larger POPC disks were generated, 7.12 ± 0.12 µm in diameter and 275 ± 10 nm in height (Figure S1).

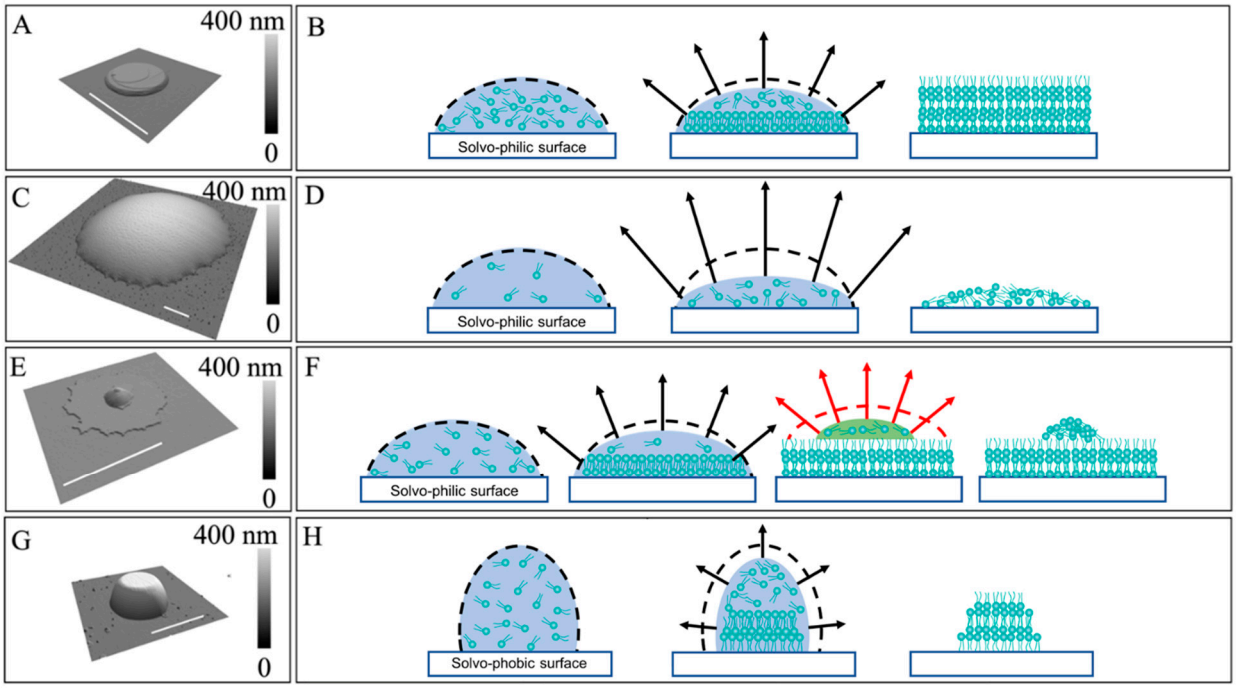


**Figure 2.** (**A**) A 3D display of an AFM topographic image of a POPC disk. (**B**) Schematic diagram illustrating the formation of (**A**), following a constant-contact area evaporation-driven assembly of POPC in a surface-supported droplet. (**C**) A 3D display of an AFM topograph of a lipid spherical cap. (**D**) Schematic diagram illustrating the formation of (**C**), following constant-contact area evaporation and trapping of POPC molecules under spatial confinement. (**E**) A 3D display of an AFM topographic image of a POPC "brimmed cap". (**F**) Schematic diagram illustrating the formation of (**E**). (**G**) A 3D display of a lipid "frustum". (**H**) Schematic diagram illustrating the formation of (**G**) under constant-contact-angle evaporation. Lateral scale bar = 2 µm.

Figure 2C shows a POPC construct with a spherical cap geometry, with a base diameter of 12.3 ± 0.6 µm and a height of 158.7 ± 6.7 nm. In this delivery, the lipid solution was prepared following identical protocols as those in experiment 2A, but with much lower POPC and glycerol concentrations. The solvent was ethanol:glycerol = 99:1 ($v/v$), with solutes of [POPC] = $3.3 \times 10^{-6}$ M and [NBD-PE] = $3.3 \times 10^{-8}$ M. Delivery was carried out under $p$ = 300 mbar, t = 500 ms, and F = 60 nN, onto a plasma-cleaned glass substrate. A 3 × 3 array of spherical caps was first produced to demonstrate consistency. The spherical cap geometry can be rationalized by the pathways of POPC assembly during evaporation, as illustrated in Figure 2D. The transient spatial confinement, instead of inter-molecular interactions, dictated the outcome of lipid assembly in this case due to two experimental parameters. First, the POPC concentration was four orders of magnitude lower than that in experiment 2A, which reduced POPC collisions, weakening inter-molecular interactions. Additionally, the evaporation rate in experiment 2C is higher than that in Figure 2A due to

a 10-fold reduction in glycerol concentration, which prompted kinetics-driven outcomes. Collectively, the assembly of the POPC molecules reflected primarily the molecular locations trapped at the transient locations upon drying. Therefore, POPC molecules are assembled into a short spherical cap structure following the spatial confinement during evaporation. The robustness of these observations was demonstrated by forming narrower and taller POPC spherical caps on less solvo-philic surfaces, such as an OTS/glass SAM, where the contact angle measured 39°. Under the same delivery conditions, the spherical caps (Figure S2) were 3.46 ± 0.49 μm at the base and 527 ± 49 nm in height, which were narrower and taller than that in Figure 2C.

At POPC concentrations of $3.3 \times 10^{-3}$ M, i.e., lower than Figure 2A, and higher than Figure 2C, and using the same solvent as that in Figure 2A, a "brimmed hat" geometry shown in Figure 2E was generated, which could be understood as a spherical cap similar to Figure 2C atop a disk analogous to Figure 2A. At $p$ = 10 mbar, t = 10 ms, and F = 75 nN, a 3 × 3 array was delivered. Each feature exhibits a 2.19 ± 0.11 μm wide and 7.2 ± 0.4 nm thick disk with a spherical cap of 1.22 ± 0.25 μm in diameter and 56.9 ± 2.3 nm tall atop the disk, as shown in Figure 2E. The disk was formed during the initial droplet spreading and constant area evaporation, as illustrated in Figure 2B. As a result, the POPC concentration was significantly depleted, and the remaining POPC assembly followed a similar pathway, as illustrated in Figure 2D, leading to a spherical cap with a base diameter of 1.22 ± 0.25 μm atop the disk. This pathway is illustrated in Figure 2F.

The impact of the initial droplet shape was also tested, e.g., using an OTS SAM surface and a solvent of ethanol:water:glycerol = 9:81:10 ($v/v$). The contact angle of our solution on the OTS SAM measured 98°, i.e., a solvo-phobic situation. Therefore, the initial droplet would bead up instead of spreading [24,58] and then evaporate following constant-contact angle evaporation [55,59,60], as shown in Figure 2H. Under a [POPC] concentration of $3.3 \times 10^{-3}$ M and delivery conditions of $p$ = 10 mbar, t =10 ms, and F = 52 nN, the POPC molecules assembled into a "frustum" or de-capped cone structures, as shown in Figure 2G. These lipid frustums measured 232.4 ± 14.3 nm tall, with base and top diameters of 2.30 ± 0.30 μm and 1.04 ± 0.19 μm, respectively. The addition of water to the mixed solvent was known to reduce the evaporation rate [28,29]. As a result, the POPC would assemble into a hat or a truncated-hat geometry, depending on the amount of POPC within. In the case of Figure 2G, a truncated hat, or solid lipid frustum, was produced. The outcome was repeated nine times in a 3 × 3 array. To demonstrate robustness, we used the same OTS/glass substrate but changed the solvent to ethanol:glycerol = 9:1 ($v/v$), i.e., removed water. The contact angle measured 39°; hence, a solvo-philic situation. In contrast to the frustum, a disk 9.92 ± 0.53 μm in base diameter and 68.2 ± 0.7 nm in height was produced (Figure S3), which was consistent with the constant-area evaporation pathway [55–57].

The molecular packing within the POPC disks was also investigated using the same printing formulation as Figure 2A. Under $p$ = −50 mbar, t = 10 ms, and F = 70 nN, POPC short disks were produced, as shown in Figure 3A, with a diameter of 1.09 ± 0.01 μm and a height of 27.6 ± 0.8 nm. Several step features are clearly visible in the zoom-in AFM topographic image in Figure 3B. The individual step height was measured from the cursor profile shown in Figure 3C: 4.9, 4.5, 4.4 nm, and 13.3 nm, respectively. In this experiment, the single step heights for all nine features in the 3 × 3 array were measured to be 4.7 ± 0.3 nm, which corresponded well with the value of POPC bilayer thickness of 4.5 nm measured via a combination of volumetric measurements and X-ray scattering [16], as well as AFM [32]. As shown in Figure 3B, the top lipid bilayer has an edge that measured 128.7 ± 2.5°, which was close to the characteristic angle (i.e., 120°) for a closely packed 2D symmetry. The formation of lipid bilayer stacks originates from strong inter-molecule interactions. The packing of high-concentration POPC under dynamic spatial confinement due to evaporation was simulated using molecular dynamics (MD) simulations in the MARTINI model, and the lipid molecules were found to assemble into gel-phased structures [32,61], consistent with the stacking of bilayers directly visualized in our experiments. Contrarily, no gel-phased structures were revealed for POPC constructs with the spherical cap geometry.

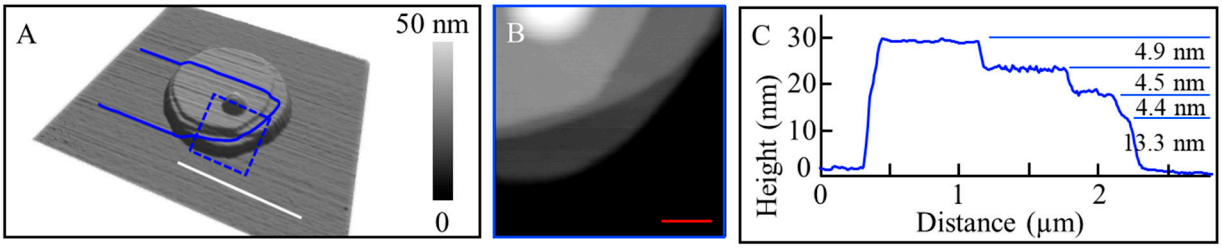


**Figure 3.** (**A**) A 3D display of an AFM topographic image of a POPC feature with the disk geometry. (**B**) A zoom-in AFM topographic image indicated by the blue square in (**A**). (**C**) Cursor profile indicated by the blue line in (**A**). White scale bar = 1 μm; red scale bar = 100 nm.

### *3.2. Producing Asymmetric Lipid Constructs*

Producing constructs with asymmetric shapes could be attained by perturbing the initial droplet shape to deviate from the symmetric spherical hat geometry driven by the surface tensions. An easy means is to tilt the probe, e.g., 11° from surface normal, inside the droplet in conjunction with extending probe time within the droplet, e.g., controlling the pulling rate. Two examples of this approach are shown in Figure 4. The lipid solution was prepared by dissolving POPC in ethanol to reach a final concentration [POPC] = $3.3 \times 10^{-2}$ M. OTS/glass SAMs were utilized in both experiments, providing solvo-phillic surfaces, where the contact angle measured 39°. Delivery of the lipid solution was performed under $p$ = 10 mbar and a contact force F = 72 nN. Upon dispensing a droplet, the probe was kept in contact with the surface for 10 ms, followed by pulling the probe up at 5 μm/s until a full and complete separation, e.g., 10 μm above the surface.

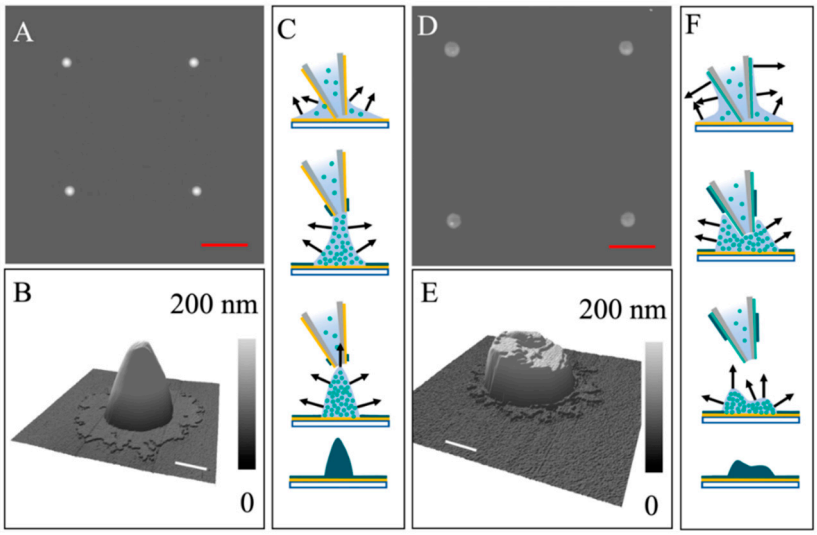


**Figure 4.** (**A**) AFM topographic image of a 2 × 2 array of lipid constructs exhibiting a shape that resembles a "traffic cone". (**B**) A 3D display of a single feature from (**A**). (**C**) Schematic diagram illustrating key moments during the probe retreat (top to bottom). The black arrows indicate the evaporation rate and direction. Yellow: OTS coating; Light teal: dissolved POPC; Dark teal: solidified POPC. (**D**) AFM topographic image of a 2 × 2 array of lipid constructs exhibiting a "bean bag" geometry. (**E**) A 3D display of a single feature from (**D**). (**F**) Schematic diagram illustrating key moments during the probe retreat (top to bottom). The black arrows indicate the evaporation rate and direction. Red scale bars = 5 μm. White scale bars = 500 nm.

Using an OTS-coated probe, Figure 4A showed a 2 × 2 array of lipid constructs produced, all exhibiting a "traffic cone" geometry with the top being slightly asymmetric. A zoom-in and 3D display shown in Figure 4B more clearly revealed the geometry and dimensions. Each lipid "traffic cone" had an overall height measured 265.5 ± 5.3 nm

and a cone base diameter of 1.48 ± 0.10 μm. At the base, a brim surrounding the cone was observed with 2.05 ± 0.18 μm in utmost diameter, width of 0.40 ± 0.08 μm, and 5.7 ± 0.4 nm in thickness. The possible pathway leading to this geometry is illustrated in Figure 4C. Upon delivery of a liquid droplet, the lipid solution spread on the surface, as well as "climbing up" the exterior of the probe. Constant-area evaporation occurred, leading to the brim of the cone on the supporting substrate. The thickness of the POPC brim measures 5.7 ± 0.4 nm. With the lifting of the probe and solvent evaporation, the droplet was constantly reshaping, becoming narrower and more elongated than the initial one. In the meantime, the POPC assembled following the triple-phase boundary confinement. With tip-droplet separation and drying, lipid features with a "traffic cone" geometry formed, as shown in Figure 4C. The robustness of the method was verified by repeating the experiment with one change in formulation, i.e., adding 10% glycerol, resulting in [POPC] = 3.3 × $10^{-2}$ M in ethanol:glycerol = 9:1 ($v/v$). The contact angle was near zero on OTS/glass. With the same probe coating, as well as delivery conditions, symmetric lipid disks are produced: base diameter = 2.37 ± 0.09 μm and height = 64.3 ± 2.6 nm (Figure S4). We attribute the formation of the lipid disks to the slower evaporation due to the higher glycerol concentration. After probe withdrawal, the droplet also had sufficient time to relax to a spherical cap shape, as dictated by surface tension. Constant contact area evaporation occurred, leading to the formation of lipid disks, similar to that shown in experiment 2A.

With a POPC-coated probe and the same delivery conditions, asymmetric lipid constructs formed, exhibiting a "brimmed bean bag" geometry, as shown in Figure 4D. A zoom-in and 3D view of a single feature is shown in Figure 4E, from which the height measures 63.8 ± 5.6 nm on the shorter side and 123.2 ± 11.5 nm on the taller side; the bean bag has a base diameter of 1.85 ± 0.06 μm. The brim measured 2.22 ± 0.24 μm in utmost diameter, 0.25 ± 0.14 μm wide, and 5.5 ± 0.3 nm in thickness. The possible pathway leading to this geometry is illustrated in Figure 4F. Upon delivery of a liquid droplet, the lipid solution spread on the surface similar to that in Figure 4C, while "climb up" is higher along the exterior of the probe due to the high solvo-philicity. Due to the 11° tilting angle of the probe, the initial droplet exhibited an asymmetric shape [28,29]. The brim formation is similar to that in experiment 4C. As the probe retreated from the liquid droplet, the droplet was constantly reshaping, becoming narrower and more elongated than the initial one. The difference was that the initial POPC molecules assembly at the exterior of the probe was faster, causing the droplet to recede along the probe exterior, leading to earlier separation than that in experiment 4C. At that moment, the asymmetry of the transient droplet was retained during the subsequent evaporation, trapping the POPC molecules within the transient droplet shape, i.e., the formation of an asymmetric lipid construct with a distinctive "bean bag" geometry.

### *3.3. Assemble Lipid Molecules by Design via Perturbing Individual Droplet During Drying*

Previous sections revealed that the initial shape of droplets significantly impacted the final geometry of POPC micro-constructs. This section explores the impact of the transient shape of droplets during drying. Taking advantage of our setup, the probe could be moved rapidly during the delivery and drying following the designed trajectories with nanometer precision [32]. In the experiments shown in Figure 5, the same surface support and lipid formulation as that in Figure 4 were used with printing conditions: $p$ = 10 mbar; t = 10 ms; and F = 50 nN. Immediately following the droplet delivery, the probe remained inside the droplet and in contact with the surface under a delivery pressure $p = -250$ mbar and a contact force of 50 nN. At the same time, the probe was continuously moving following predesigned time-dependent positions, i.e., X(t) and Y(t). An example of the X(t) and Y(t) is shown in Figure 5B, which led to a probe movement along a micro-cross with each arm being 3 μm long. After the movement in the X-Y plane, the probe withdrew from the droplet. Upon solvent evaporation, POPC molecules in each droplet assembled into a micro-cross, where a 2 × 2 array is shown in Figure 5C. One of the representative lipid crosses was shown in Figure 5D, where the arms measured 3.27 ± 0.16 μm in length and

1.57 ± 0.14 µm in full width at half maximum (FWHM). The feature height measured 685 ± 41 nm in the center and 574 ± 50 nm in the arms. The cross-section measured 2.82 ± 0.34 µm in width.

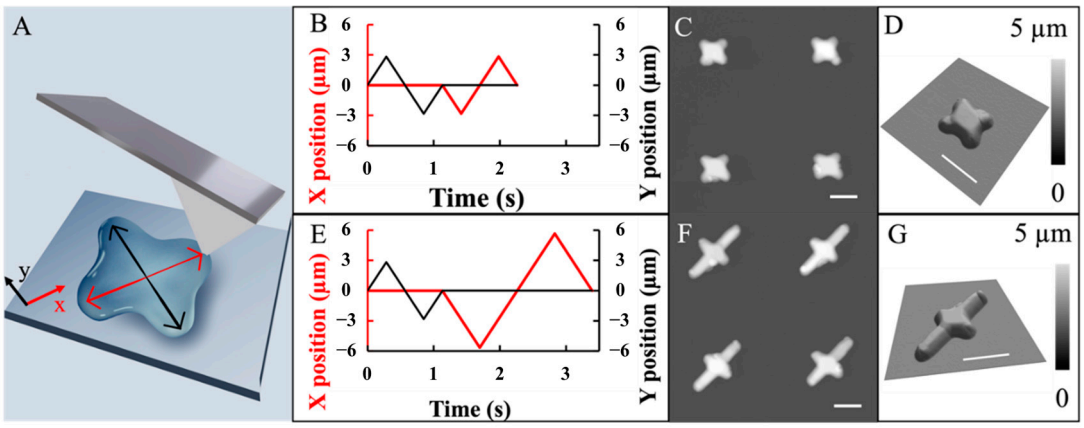


**Figure 5.** (**A**) Schematic diagram illustrating the concept of perturbing individual liquid droplet shapes via tip movement (double arrow black and red lines). (**B**) Programmed X and Y positions of the probe plotted as a function of time. The center of the droplet was the origin of the coordinate. (**C**) AFM topographic image of a 2 × 2 array of POPC micro-crosses. Each droplet was perturbed following tip trajectory designed in (**B**). (**D**) A 3D display of the top left cross from (**C**). (**E**) Programmed X and Y positions of the probe plotted as a function of time. The center of the droplet was the origin of the coordinate. (**F**) AFM topographic image of a 2 × 2 array of asymmetric POPC crosses. (**G**) A 3D display of the top left feature from (**F**). Scale bar = 5 µm.

The robustness of this approach is demonstrated by guiding the POPC molecules to assemble into an asymmetrical cross as designed. With the X(t) and Y(t) designed in Figure 5E, the probe moved along an asymmetrical cross with arm length being 6 and 3 µm, respectively. POPC assembled into asymmetric crosses, as exampled in Figure 5F, where a 2 × 2 array is displayed. One typical asymmetric cross is shown in Figure 5G, from which the long and short arms measured 6.11 ± 0.40 µm and 3.18 ± 0.24 µm in length, respectively. The width was 1.68 ± 0.10 µm (FWHM), and the feature height measured 687 ± 88 nm in the center and 547 ± 88 nm in the arms. The cross-section measured 2.14 ± 0.28 µm in width.

Both the symmetric and asymmetric crosses were repeated at least eight times in two independent experiment sets to ensure consistent and reproducible results. These results demonstrated the concept of control over the assembly of lipid molecules into designed geometries by actively perturbing the droplet at a designed trajectory during drying. In contrast to the conventional drop-and-dry approach where symmetric constructs were typically generated [62,63], our method actively reshapes the droplet by our programmed trajectory during solvent evaporation and, as such, allows for the production of non-equilibrium structures of lipid assembly constructed by design. To the best of our knowledge, this is the first time that active reshaping of individual droplets was adopted to produce 3D micro- and nanostructures.

### *3.4. 3D Nanoprinting of Lipid Molecules*

In principle, with successful 0D printing of a lipid, it should be feasible to make concrete 0D features continuous, i.e., 1D printing. By the same token, connecting lines into planes enables 2D printing, and stacking designed 2D structures should attain 3D constructs. With conditions of 0D printing, i.e., controlling assembly of POPC in a droplet, at hand, we moved further to attempt the 3D nanoprinting of a lipid. Figure 6 demonstrates the proof of concept using a design with 5-fold symmetry, as illustrated in Figure 6A.

Features with a five-fold symmetry are difficult to attain in nature or via self-assembly but should, in principle, be routine in our approach.

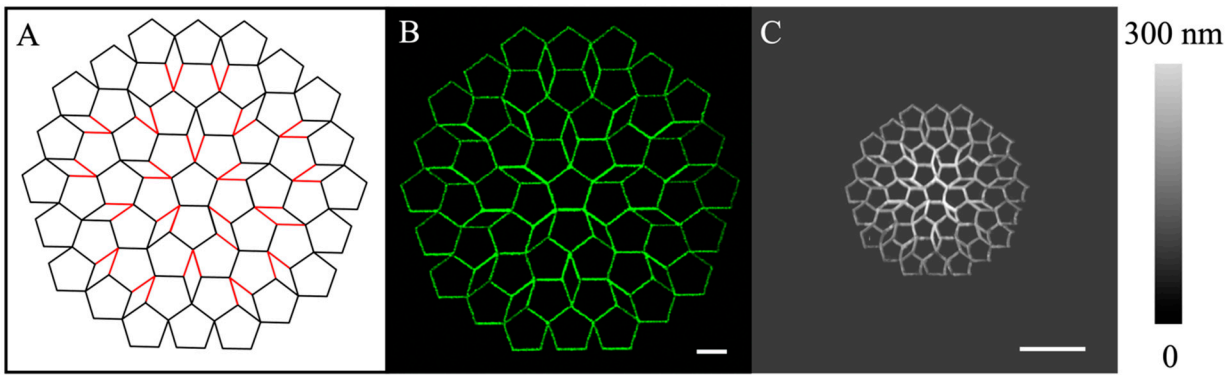


**Figure 6.** (**A**) The design of a structure with 5-fold symmetry, consisting of connected pentagons and diamonds with equal side lengths. The black and red lines represent the one pass and two passes during the delivery, respectively. (**B**) Confocal image revealing the outcome of a 3D printing of POPC following the design in (**A**), with individual pentagon side length set at 20 µm. (**C**) AFM topographic image of the resulting 3D printing of POPC following the same design and with individual pentagon side lengths set at 5 µm. Scale bar = 20 µm.

This design originated with a central pentagon and expanded outward with more pentagons. The entire pattern consisted of 51 identical pentagons and 20 diamonds connecting these pentagons. The support surface is an OTS/glass, and the printing solution formulation is the same as that in Figures 4 and 5: [POPC] = $3.3 \times 10^{-2}$ M, [NBD-PE] = $3.3 \times 10^{-4}$ M in ethanol. Two representative POPC patterns, shown in Figure 6B,C, were printed following the design shown in Figure 6A, with individual pentagon side lengths of 20 µm and 5 µm, respectively. To produce the designed patterns, the probe was first brought into contact with the surface until the set force of F = 50 nN. The probe's programmed movement was promptly initiated, following the trajectory, as depicted in Figure 6A. For the POPC pattern in Figure 6B, printing started at the top point of the central pentagon and then followed the line trajectory of the first pentagon, as shown in Figure 6A. The contact force was maintained at F = 50 nN, i.e., the delivery probe followed the designed trajectory while maintaining consistent contact with the supporting surface. After attempting various delivery pressures, we kept $p = -250$ mbar at the printing speed of 10 µm/s to avoid uncontrolled solution spreading, aka over-delivery on the solvo-philic surface, or lack of designed material delivery. Upon completion of the designed paths (all lines in Figure 6A), the probe was lifted. The final POPC assemblies followed the design with high fidelity, as shown in Figure 6B. Each line measures 20.0 µm long, with line width = 1.3–1.4 µm and line height = 218–496 nm. The footprint of the pattern covered a 230 µm × 242 µm region. The sides with double passes appeared taller than those produced via single passes, as anticipated.

Further miniaturization of this design was also attempted. One example is shown in Figure 6C, where the individual pentagon side length = 5 µm. Printing conditions followed that shown in experiment 6B, except that the delivery speed was set to 2 µm/s. The lines measured 108–240 nm in height and 788–960 nm in width. The pattern covers 57.5 µm × 60.5 µm area. The reproducibility of the pattern was demonstrated by repeating the printing multiple times during two separate experiments. We observed structural characteristics specifically pertaining to our methodology. The center pentagons were brighter than the outside pentagons, which is consistent with the higher initial flow of the lipid solution from the probe than the subsequent delivery. Lines near horizontal directions were slightly taller than other lines due to the direction dependence of our delivery configuration [53]. Occasionally, corners exhibited build-ups due to material

accumulation at a turning point. Work is in progress to optimize delivery conditions and configuration to improve this technology further.

## 4. Conclusions

Integrating AFM with microfluidic delivery, this work enables controlled assembly of amphiphilic lipid molecules such as 1-palmitoyl-2-oleoyl-*sn*-glycero-3-phosphocholine (POPC). By moving the probe following the designed trajectory upon dispensing and during drying, the transient shape of the small liquid droplets is regulated. In doing so, the shape of the POPC assembly has been regulated to the designed geometry with high spatial precision. Examples of lipid constructs achieved with designed shapes include disks, traffic cones, "bean bag", and symmetric and asymmetric micro-cross. Built upon this concept, POPC assemblies in 3D were designed and built, including constructs with a five-fold symmetry. Work is in progress to further improve the precision in material delivery and to explore applications in drug delivery and additive manufacturing via 3D nanoprinting. Future work will also include extending this approach to a broad range of amphiphilic molecules and formulations. The concept of controlled assembly of lipids demonstrated in this work also facilitates the development of lipid-based functional biomaterials, sensors, and devices.

**Supplementary Materials:** The following supporting information can be downloaded at: https://www.mdpi.com/article/10.3390/chemistry6050074/s1, Figures S1–S4: AFM topographic images demonstrating the robustness of controlled assembly of lipid molecules via regulating transient spatial confinement.

**Author Contributions:** Conceptualization, G.-Y.L.; formal analysis, Y.H. and Z.X.; funding acquisition, G.-Y.L.; investigation, Y.H., U.C. and Z.X.; methodology, G.-Y.L., U.C. and Y.H.; project administration, G.-Y.L.; resources, Y.H., Z.X. and D.S.; software, D.O.; supervision, G.-Y.L.; validation, Y.H. and Z.X.; visualization, Y.H. and Z.X.; writing—original draft, Y.H.; writing—review and editing, Y.H., Z.X., D.O., R.F., A.N.P. and G.-Y.L. All authors have read and agreed to the published version of the manuscript.

**Funding:** This work is supported by U.C. Davis and the National Science Foundation (CHE-2304986).

**Data Availability Statement:** The original contributions and data presented in the study are available upon specific request. Please contact the corresponding author if needed.

**Acknowledgments:** The authors wish George Whitesides a very happy birthday. His pioneer and comprehensive work on self-assembly of molecules is the inspiration for the present work. The authors appreciate helpful discussions with Arpad Karsai, Bradley S. Harris, Yunbo Zheng, Christopher F. Carnahan, and Saswati Panda. We thank Pallavi D. Sambre for her assistance in preparing the lipid sample and Susan Stagner for her careful proofreading of this article. We appreciate the critiques by both reviewers, which helped improve the quality and clarity of this paper. The laser scanning confocal microscopy was performed in the Keck Spectral Imaging Facility of U.C. Davis. The initial technology was developed with the support of the Gordon and Betty Moore Foundation. This publication is based upon work supported by (while the corresponding author serving at) the National Science Foundation.

**Conflicts of Interest:** The authors declare no conflicts of interest.

## References

1. Bogdanov, M.; Mileykovskaya, E.; Dowhan, W. Lipids in the assembly of membrane proteins and organization of protein supercomplexes: Implications for lipid-linked disorders. *Sub-Cell. Biochem.* **2008**, *49*, 197–239. [CrossRef]
2. Mouritsen, O.G. Self-assembly and organization of lipid-protein membranes. *Curr. Opin. Colloid Interface Sci.* **1998**, *3*, 78–87. [CrossRef]
3. Kholodenko, B.N. Cell-signalling dynamics in time and space. *Nat. Rev. Mol. Cell Biol.* **2006**, *7*, 165–176. [CrossRef] [PubMed]
4. Meikle, T.G.; Zabara, A.; Waddington, L.J.; Separovic, F.; Drummond, C.J.; Conn, C.E. Incorporation of antimicrobial peptides in nanostructured lipid membrane mimetic bilayer cubosomes. *Colloids Surf. B Biointerfaces* **2017**, *152*, 143–151. [CrossRef]
5. Kulkarni, C.V. Lipid crystallization: From self-assembly to hierarchical and biological ordering. *Nanoscale* **2012**, *4*, 5779–5791. [CrossRef]

6. Conn, C.E.; Drummond, C.J. Nanostructured bicontinuous cubic lipid self-assembly materials as matrices for protein encapsulation. *Soft Matter* **2013**, *9*, 3449–3464. [CrossRef]
7. Nagle, J.F. Theory of the Main Lipid Bilayer Phase Transition. *Annu. Rev. Phys. Chem.* **1980**, *31*, 157–196. [CrossRef]
8. Israelachvili, J.N.; Mitchell, D.J.; Ninham, B.W. Theory of self-assembly of lipid bilayers and vesicles. *Biochim. Biophys. Acta (BBA)-Biomembr.* **1977**, *470*, 185–201. [CrossRef]
9. Kusi-Appiah, A.E.; Vafai, N.; Cranfill, P.J.; Davidson, M.W.; Lenhert, S. Lipid multilayer microarrays for in vitro liposomal drug delivery and screening. *Biomaterials* **2012**, *33*, 4187–4194. [CrossRef]
10. Reimhult, E.; Kumar, K. Membrane biosensor platforms using nano- and microporous supports. *Trends Biotechnol.* **2008**, *26*, 82–89. [CrossRef]
11. Su, H.; Liu, H.-Y.; Pappa, A.-M.; Hidalgo, T.C.; Cavassin, P.; Inal, S.; Owens, R.M.; Daniel, S. Facile Generation of Biomimetic-Supported Lipid Bilayers on Conducting Polymer Surfaces for Membrane Biosensing. *ACS Appl. Mater. Interfaces* **2019**, *11*, 43799–43810. [CrossRef] [PubMed]
12. Shanmugam, T.; Banerjee, R. Nanostructured self assembled lipid materials for drug delivery and tissue engineering. *Ther. Deliv.* **2011**, *2*, 1485–1516. [CrossRef]
13. Dixon, J.B.; Raghunathan, S.; Swartz, M.A. A tissue-engineered model of the intestinal lacteal for evaluating lipid transport by lymphatics. *Biotechnol. Bioeng.* **2009**, *103*, 1224–1235. [CrossRef]
14. Monteiro, N.; Martins, A.; Reis, R.L.; Neves, N.M. Liposomes in tissue engineering and regenerative medicine. *J. R. Soc. Interface* **2014**, *11*, 20140459. [CrossRef]
15. Yang, T.; Jung, S.-y.; Mao, H.; Cremer, P.S. Fabrication of Phospholipid Bilayer-Coated Microchannels for On-Chip Immunoassays. *Anal. Chem.* **2001**, *73*, 165–169. [CrossRef] [PubMed]
16. Kucerka, N.; Liu, Y.; Chu, N.; Petrache, H.I.; Tristram-Nagle, S.; Nagle, J.F. Structure of fully hydrated fluid phase DMPC and DLPC lipid bilayers using X-ray scattering from oriented multilamellar arrays and from unilamellar vesicles. *Biophys. J.* **2005**, *88*, 2626–2637. [CrossRef]
17. Roberts, G.G. An applied science perspective of Langmuir-Blodgett films. *Adv. Phys.* **1985**, *34*, 475–512. [CrossRef]
18. Pockels, A. On the Spreading of Oil upon Water. *Nature* **1894**, *50*, 223–224. [CrossRef]
19. Lind, T.K.; Cárdenas, M.; Wacklin, H.P. Formation of Supported Lipid Bilayers by Vesicle Fusion: Effect of Deposition Temperature. *Langmuir* **2014**, *30*, 7259–7263. [CrossRef]
20. Chen, X.; Lenhert, S.; Hirtz, M.; Lu, N.; Fuchs, H.; Chi, L. Langmuir–Blodgett Patterning: A Bottom–Up Way To Build Mesostructures over Large Areas. *Acc. Chem. Res.* **2007**, *40*, 393–401. [CrossRef]
21. Xu, S.; Liu, G.-y. Nanometer-Scale Fabrication by Simultaneous Nanoshaving and Molecular Self-Assembly. *Langmuir* **1997**, *13*, 127–129. [CrossRef]
22. Urtizberea, A.; Hirtz, M. A diffusive ink transport model for lipid dip-pen nanolithography. *Nanoscale* **2015**, *7*, 15618–15634. [CrossRef]
23. Lenhert, S.; Sun, P.; Wang, Y.; Fuchs, H.; Mirkin, C.A. Massively parallel dip-pen nanolithography of heterogeneous supported phospholipid multilayer patterns. *Small* **2007**, *3*, 71–75. [CrossRef]
24. Gavutis, M.; Navikas, V.; Rakickas, T.; Vaitekonis, Š.; Valiokas, R. Lipid dip-pen nanolithography on self-assembled monolayers. *J. Micromechanics Microengineering* **2016**, *26*, 025016. [CrossRef]
25. Hirtz, M.; Oikonomou, A.; Georgiou, T.; Fuchs, H.; Vijayaraghavan, A. Multiplexed biomimetic lipid membranes on graphene by dip-pen nanolithography. *Nat. Commun.* **2013**, *4*, 2591. [CrossRef] [PubMed]
26. Hovis, J.S.; Boxer, S.G. Patterning and Composition Arrays of Supported Lipid Bilayers by Microcontact Printing. *Langmuir* **2001**, *17*, 3400–3405. [CrossRef]
27. Sekula-Neuner, S.; de Freitas, M.; Tröster, L.-M.; Jochum, T.; Levkin, P.A.; Hirtz, M.; Fuchs, H. Phospholipid arrays on porous polymer coatings generated by micro-contact spotting. *Beilstein J. Nanotechnol.* **2017**, *8*, 715–722. [CrossRef]
28. Zhang, J.; Piunova, V.A.; Liu, Y.; Tek, A.; Yang, Q.; Frommer, J.; Liu, G.-y.; Sly, J. Controlled Molecular Assembly via Dynamic Confinement of Solvent. *J. Phys. Chem. Lett.* **2018**, *9*, 6232–6237. [CrossRef]
29. Zhang, J.; Yu, H.; Harris, B.; Zheng, Y.; Celik, U.; Na, L.; Faller, R.; Chen, X.; Haudenschild, D.R.; Liu, G.-y. New Means to Control Molecular Assembly. *J. Phys. Chem. C* **2020**, *124*, 6405–6412. [CrossRef]
30. Wang, S.; Liu, S.; Sulkanen, A.; Fox Joseph, M.; Jia, X.; Liu, G.-y. Controlled Molecular Assembly of Tetrazine Derivatives on Surfaces. *CCS Chem.* **2021**, *4*, 162–172. [CrossRef]
31. Pattison, T.G.; Wang, S.; Miller, R.D.; Liu, G.-y.; Qiao, G.G. 3D nanoprinting via spatially controlled assembly and polymerization. *Nat. Commun.* **2022**, *13*, 1941. [CrossRef] [PubMed]
32. Huang, Y.; Karsai, A.; Sambre, P.D.; Su, W.-C.; Faller, R.; Parikh, A.N.; Liu, G.-Y. Production of Lipid Constructs by Design via Three-Dimensional Nanoprinting. *Micromachines* **2023**, *14*, 372. [CrossRef] [PubMed]
33. Meister, A.; Gabi, M.; Behr, P.; Studer, P.; Vörös, J.; Niedermann, P.; Bitterli, J.; Polesel-Maris, J.; Liley, M.; Heinzelmann, H.; et al. FluidFM: Combining Atomic Force Microscopy and Nanofluidics in a Universal Liquid Delivery System for Single Cell Applications and Beyond. *Nano Lett.* **2009**, *9*, 2501–2507. [CrossRef]
34. Fabié, L.; Ondarçuhu, T. Writing with liquid using a nanodispenser: Spreading dynamics at the sub-micron scale. *Soft Matter* **2012**, *8*, 4995–5001. [CrossRef]

35. Meister, A.; Liley, M.; Brugger, J.; Pugin, R.; Heinzelmann, H. Nanodispenser for attoliter volume deposition using atomic force microscopy probes modified by focused-ion-beam milling. *Appl. Phys. Lett.* **2004**, *85*, 6260–6262. [CrossRef]
36. Wei, T.; Huang, T.; Qiao, B.; Zhang, M.; Ma, H.; Zhang, L. Structures, Dynamics, and Water Permeation Free Energy across Bilayers of Lipid A and Its Analog Studied with Molecular Dynamics Simulation. *J. Phys. Chem. B* **2014**, *118*, 13202–13209. [CrossRef]
37. Walde, P.; Ichikawa, S. Enzymes inside lipid vesicles: Preparation, reactivity and applications. *Biomol. Eng.* **2001**, *18*, 143–177. [CrossRef]
38. Tieleman, D.P.; Forrest, L.R.; Sansom, M.S.P.; Berendsen, H.J.C. Lipid Properties and the Orientation of Aromatic Residues in OmpF, Influenza M2, and Alamethicin Systems: Molecular Dynamics Simulations. *Biochemistry* **1998**, *37*, 17554–17561. [CrossRef]
39. Berganza, E.; Hirtz, M. Direct-Write Patterning of Biomimetic Lipid Membranes In Situ with FluidFM. *ACS Appl. Mater. Interfaces* **2021**, *13*, 50774–50784. [CrossRef]
40. Smith, K.A.; Gale, B.K.; Conboy, J.C. Micropatterned Fluid Lipid Bilayer Arrays Created Using a Continuous Flow Microspotter. *Anal. Chem.* **2008**, *80*, 7980–7987. [CrossRef]
41. Lin, W.-F.; Swartz, L.A.; Li, J.-R.; Liu, Y.; Liu, G.-Y. Particle Lithography Enables Fabrication of Multicomponent Nanostructures. *J. Phys. Chem. C* **2013**, *117*, 23279–23285. [CrossRef] [PubMed]
42. Lin, W.-F.; Li, J.-R.; Liu, G.-Y. Near-Field Scanning Optical Microscopy Enables Direct Observation of Moiré Effects at the Nanometer Scale. *ACS Nano* **2012**, *6*, 9141–9149. [CrossRef]
43. Li, J.-R.; Garno, J.C. Elucidating the Role of Surface Hydrolysis in Preparing Organosilane Nanostructures via Particle Lithography. *Nano Lett.* **2008**, *8*, 1916–1922. [CrossRef] [PubMed]
44. Liu, Y.; Wang, K.-H.; Chen, H.-Y.; Li, J.-R.; Laurence, T.A.; Ly, S.; Liu, F.-T.; Liu, G.-Y. Periodic Arrangement of Lipopolysaccharides Nanostructures Accelerates and Enhances the Maturation Processes of Dendritic Cells. *ACS Appl. Nano Mater.* **2018**, *1*, 839–850. [CrossRef]
45. Li, J.-R.; Lusker, K.L.; Yu, J.-J.; Garno, J.C. Engineering the Spatial Selectivity of Surfaces at the Nanoscale Using Particle Lithography Combined with Vapor Deposition of Organosilanes. *ACS Nano* **2009**, *3*, 2023–2035. [CrossRef] [PubMed]
46. Yuan, W.; van Ooij, W.J. Characterization of Organofunctional Silane Films on Zinc Substrates. *J. Colloid Interface Sci.* **1997**, *185*, 197–209. [CrossRef]
47. Abbott, N.L.; Gorman, C.B.; Whitesides, G.M. Active Control of Wetting Using Applied Electrical Potentials and Self- Assembled Monolayers. *Langmuir* **1995**, *11*, 16–18. [CrossRef]
48. Bain, C.D.; Whitesides, G.M. A study by contact angle of the acid-base behavior of monolayers containing .omega.-mercaptocarboxylic acids adsorbed on gold: An example of reactive spreading. *Langmuir* **1989**, *5*, 1370–1378. [CrossRef]
49. Grüter, R.R.; Vörös, J.; Zambelli, T. FluidFM as a lithography tool in liquid: Spatially controlled deposition of fluorescent nanoparticles. *Nanoscale* **2013**, *5*, 1097–1104. [CrossRef]
50. Deng, W.N.; Wang, S.; Ventrici de Souza, J.; Kuhl, T.L.; Liu, G.-Y. New Algorithm to Enable Construction and Display of 3D Structures from Scanning Probe Microscopy Images Acquired Layer-by-Layer. *J. Phys. Chem. A* **2018**, *122*, 5756–5763. [CrossRef]
51. Kang, W.; McNaughton, R.L.; Yavari, F.; Minary-Jolandan, M.; Safi, A.; Espinosa, H.D. Microfluidic parallel patterning and cellular delivery of molecules with a nanofountain probe. *J. Lab. Autom.* **2014**, *19*, 100–109. [CrossRef] [PubMed]
52. Ventrici de Souza, J.; Liu, Y.; Wang, S.; Dörig, P.; Kuhl, T.L.; Frommer, J.; Liu, G.-Y. Three-Dimensional Nanoprinting via Direct Delivery. *J. Phys. Chem. B* **2018**, *122*, 956–962. [CrossRef] [PubMed]
53. Tran, V.; Karsai, A.; Fong, M.C.; Cai, W.; Yik, J.H.N.; Klineberg, E.; Haudenschild, D.R.; Liu, G.-Y. Label-Free and Direct Visualization of Multivalent Binding of Bone Morphogenetic Protein-2 with Cartilage Oligomeric Matrix Protein. *J. Phys. Chem. B* **2019**, *123*, 39–46. [CrossRef] [PubMed]
54. Li, G.; Kim, J.; Huang, Z.; St. Clair, J.R.; Brown, D.A.; London, E. Efficient replacement of plasma membrane outer leaflet phospholipids and sphingolipids in cells with exogenous lipids. *Proc. Natl. Acad. Sci. USA* **2016**, *113*, 14025–14030. [CrossRef] [PubMed]
55. Chhasatia, V.H.; Sun, Y. Interaction of bi-dispersed particles with contact line in an evaporating colloidal drop. *Soft Matter* **2011**, *7*, 10135–10143. [CrossRef]
56. Ko, H.-Y.; Park, J.; Shin, H.; Moon, J. Rapid Self-Assembly of Monodisperse Colloidal Spheres in an Ink-Jet Printed Droplet. *Chem. Mater.* **2004**, *16*, 4212–4215. [CrossRef]
57. Park, J.; Moon, J. Control of Colloidal Particle Deposit Patterns within Picoliter Droplets Ejected by Ink-Jet Printing. *Langmuir* **2006**, *22*, 3506–3513. [CrossRef]
58. Berganza, E.; Boltynjuk, E.; Mathew, G.; Vallejo, F.F.; Gröger, R.; Scherer, T.; Sekula-Neuner, S.; Hirtz, M. 3D Nanolithography by Means of Lipid Ink Spreading Inhibition. *Small* **2023**, *19*, 2205590. [CrossRef]
59. Erbil, H.Y.; McHale, G.; Newton, M.I. Drop Evaporation on Solid Surfaces: Constant Contact Angle Mode. *Langmuir* **2002**, *18*, 2636–2641. [CrossRef]
60. Zhong, X.; Crivoi, A.; Duan, F. Sessile nanofluid droplet drying. *Adv. Colloid Interface Sci.* **2015**, *217*, 13–30. [CrossRef]
61. Harris, B.S.; Huang, Y.; Karsai, A.; Su, W.-C.; Sambre, P.D.; Parikh, A.N.; Liu, G.-Y.; Faller, R. Impact of Surface Polarity on Lipid Assembly under Spatial Confinement. *Langmuir* **2022**, *38*, 7545–7557. [CrossRef] [PubMed]

62. Guzmán, E.; Ortega, F.; Rubio, R.G. Forces Controlling the Assembly of Particles at Fluid Interfaces. *Langmuir* **2022**, *38*, 13313–13321. [CrossRef] [PubMed]
63. Young, T., III. An essay on the cohesion of fluids. *Philos. Trans. R. Soc. Lond.* **1805**, *95*, 65–87. [CrossRef]

**Disclaimer/Publisher's Note:** The statements, opinions and data contained in all publications are solely those of the individual author(s) and contributor(s) and not of MDPI and/or the editor(s). MDPI and/or the editor(s) disclaim responsibility for any injury to people or property resulting from any ideas, methods, instructions or products referred to in the content.